Electronics and Electrical Engineering

AIMS Electronics and Electrical Engineering, 9(2): 215–242.
DOI: 10.3934/electreng.2025011
Received: 20 December 2024
Revised: 21 March 2025
Accepted: 02 April 2025
Published: 15 April 2025

http://www.aimspress.com/journal/ElectrEng

*Research article*

# Reduction of harmonic distortion in electromagnetic torque of a single-phase reluctance motor using a multilevel neutral-point-clamped DC-AC converter

**José M. Campos-Salazar[1,*], Roya Rafiezadeh[2], Juan L. Aguayo-Lazcano[3] and Constanza Márquez[4]**

[1] Electronic Engineering Department, Universitat Politècnica de Catalunya, Barcelona, Spain
[2] PEMC group, University of Nottingham, Nottingham, United Kingdom
[3] Institute of Physical and Mathematical Sciences, Universidad Austral de Chile, Valdivia, Chile
[4] Mechanical Maintenance Department, Celulosa Arauco y Constitución SA, Valdivia, Chile

*** Correspondence:** Email: jose.manuel.campos@upc.edu.

**Abstract:** The harmonic performance, control robustness, and thermal characteristics of single-phase multilevel neutral-point-clamped (NPC) converters driving a single-phase reluctance motor (SPRM) are comprehensively analyzed in this study. Three converter topologies—a two-level single-phase NPC (2L-1P-NPC) converter, a three-level single-phase NPC (3L-1P-NPC) converter, and a four-level single-phase NPC (4L-1P-NPC) converter—are investigated under four modulation schemes: bipolar voltage pulsewidth modulation (BVPWM), unipolar voltage pulsewidth modulation (UVPWM), level-shifted pulsewidth modulation (LSPWM), and virtual-vector pulsewidth modulation (VVPWM), all operating at a fixed switching frequency of 10 kHz. High-fidelity simulations conducted in MATLAB-Simulink accurately replicate the coupled electromagnetic, mechanical, and thermal dynamics of the SPRM system, utilizing realistic motor and load parameters to ensure application-level relevance.

The results demonstrate that increasing the converter level substantially reduces total harmonic distortion (THD), with the 4L-1P-NPC topology under LSPWM achieving the lowest THD of 23.66%, thereby significantly improving voltage waveform quality and minimizing electromagnetic torque ripple. A proportional–integral (PI)-based feedback controller is implemented for velocity and position regulation, yielding precise trajectory tracking, a fast transient response, and negligible steady-state error. Additionally, thermal analysis quantifies power losses—conduction, switching,

core, and copper—highlighting the trade-off between improved harmonic/dynamic performance and increased thermal stress. Notably, the junction temperature escalates from 121.8 ℃ in the 2L-1P-NPC converter to 188 ℃ in the 4L-1P-NPC converter, underscoring the necessity for advanced heat dissipation strategies in high-power applications.

By integrating harmonic distortion mitigation, closed-loop control design, and thermal evaluation, this work presents a unified framework for the optimal design and analysis of high-performance, thermally aware multilevel SPRM drives.

**Keywords:** angular position; harmonic distortion; multilevel converters; proportional–integral control; single-phase reluctance motor; thermal analysis

## 1. Introduction

In response to the growing demand for enhanced efficiency in industrial electric motor drive systems, the implementation of systems based on solid-state components is becoming increasingly prevalent. Despite their advantages, these systems introduce nonsinusoidal voltage and current waveforms at their output terminals, which contain numerous harmonic components. These harmonics degrade the motor's performance and subsequently affect the coupled mechanical load, leading to issues such as electromagnetic interference, audible noise, and vibrations [1]. Specifically, in AC machines, the generation of noise is closely related to the radial forces, which are directly proportional to the air-gap flux density. Thus, by mitigating the magnitude of this density, noise can be reduced. Additionally, rotors with low skew angles tend to generate higher levels of noise and vibrations [2–15]. Notably, while high-frequency operation of drive systems may reduce acoustic noise, it could simultaneously induce mechanical resonances within the system [15,16].

The harmonic content in the output currents of solid-state drives produces nonsinusoidal magnetomotive force (mmf) waveforms, which, in turn, result in electromagnetic torque containing additional harmonics [1]. These harmonics within the electromagnetic torque can be classified into two distinct categories: stationary harmonic torques and pulsating harmonic torques [1]. Stationary harmonics arise from the interaction between harmonics of the rotor's mmf and harmonics of the same order in the air-gap flux [1,17]. On the other hand, pulsating harmonic torques are induced by the interaction of the rotor's mmf harmonics with those of different orders in the rotating air-gap flux harmonics [1,17]. It is noteworthy that lower-order pulsating torques can be mitigated by employing drive systems with pulsewidth modulation switching strategies [18–21]. Furthermore, in AC motors operating at low speeds, drives utilizing high-frequency switching can achieve electromagnetic torque with minimal harmonic contamination [19–21].

Considering the advantages of multilevel converters, they are promising candidates for driving AC motors due to their ability to reduce harmonic distortion in output voltages and currents. However, this benefit comes at the cost of increased complexity in the control system, requiring more switching devices and sophisticated modulation techniques [22,23].

One type of AC motor, the single-phase reluctance motor (SPRM), operates on the principle of reluctance rather than induction. Unlike induction motors, which rely on slip to generate rotor flux, SPRMs operate synchronously and require a dedicated drive system for starting. The simplicity of SPRMs' construction, combined with their low cost, makes them suitable for a wide range of

applications, from domestic appliances such as washing machines to large industrial pumps [17]. Despite their widespread use, the issue of harmonic distortion in the electromagnetic torque ($T_e(t)$) of SPRMs remains relatively underexplored. For instance, in [24], a nonlinear analytical model of an SPRM is presented, accounting for magnetic saturation and slotting effects. Meanwhile, in [25], an SPRM operating directly online, without the need for an external driver, is proposed as a candidate for pumping applications. Nonetheless, none of these studies addressed the impact of harmonic distortion on the SPRM's electromagnetic torque, which can significantly degrade the motor's performance.

This study presents a comprehensive harmonic and thermal evaluation of SPRM drives powered by single-phase neutral-point-clamped (NPC) multilevel DC–AC converters. Three topologies—a two-level single-phase NPC converter (2L-1P-NPC), a three-level single-phase NPC converter (3L-1P-NPC), and a four-level single-phase NPC converter (4L-1P-NPC)—are examined under four pulsewidth modulation (PWM) strategies: bipolar voltage PWM (BVPWM), unipolar voltage PWM (UVPWM), level-shifted PWM (LSPWM), and virtual-vector PWM (VVPWM), all operating at a constant 10 kHz switching frequency. Simulations in the MATLAB-Simulink environment provide high-fidelity modeling of the electromechanical dynamics, enabling accurate THD characterization in both the voltage and torque profiles.

Beyond harmonic performance, this study incorporates a comprehensive thermal analysis, evaluating switching losses ($P_{sw}$), conduction losses ($P_{cond}$), core losses ($P_{core}$), and copper losses ($P_{copper}$). Higher-level converters reduce voltage stress per switch but increase cumulative conduction losses, elevating junction temperatures ($T_j$) from 121.8 ℃ in the 2L-1P-NPC converter to 188 ℃ in the 4L-1P-NPC converter, necessitating advanced cooling strategies. While multilevel converters enhance harmonic performance, effective thermal management is crucial for maintaining the system reliability.

This work is entirely theoretical, employing MATLAB-Simulink simulations for rigorous system assessment, with experimental validation planned for future work. These findings establish a foundation for optimizing power conversion systems, balancing power quality, efficiency, and thermal performance in high-performance SPRM drives.

The article is organized as follows: Section 2 defines the converter topologies, while Section 3 models the SPRM and converters. Section 4 details the modulation strategies, and Section 5 analyzes the thermal performance. Section 6 outlines PI-based control, Section 7 presents the simulation results, and Section 8 concludes with the key findings and future directions.

## 2. The system's topology

This study analyzes three distinct topologies, all of which utilize the same SPRM, while varying the level of the single-phase DC–AC NPC converter (1P-NPC) from two to four levels. Specifically, Topologies A, B, and C correspond to the configurations where the SPRM is driven by a 1P-NPC with two, three, and four levels, respectively. Figure 1 illustrates the switching models of the 1P-NPC converters, along with the electrical circuit of the SPRM for each topology under investigation.

As shown in Figure 1, the SPRM is modeled as an electromechanical system [17,26], with its electrical circuit characterized by the stator's winding resistance ($R_a$) and inductance ($L_a(\theta_m(t))$), where the inductance is a function of the rotor's angular position ($\theta_m(t)$). The terminal voltage ($v_a(t)$),

stator current ($i_a(t)$), and developed electromagnetic torque ($T_e(t)$) are key variables of the electrical side. On the mechanical side, which remains identical across all topologies, the system is represented by a rotating load modeled via its electrical analog [27]. This mechanical load is defined by its moment of inertia ($J_L$), along with its damping ($b_L$) and stiffness coefficients ($k_L$). Additionally, the mechanical torque ($T_L(t)$) developed by the load and the angular position ($\theta_L(t)$) of the load complete the description of the mechanical subsystem.

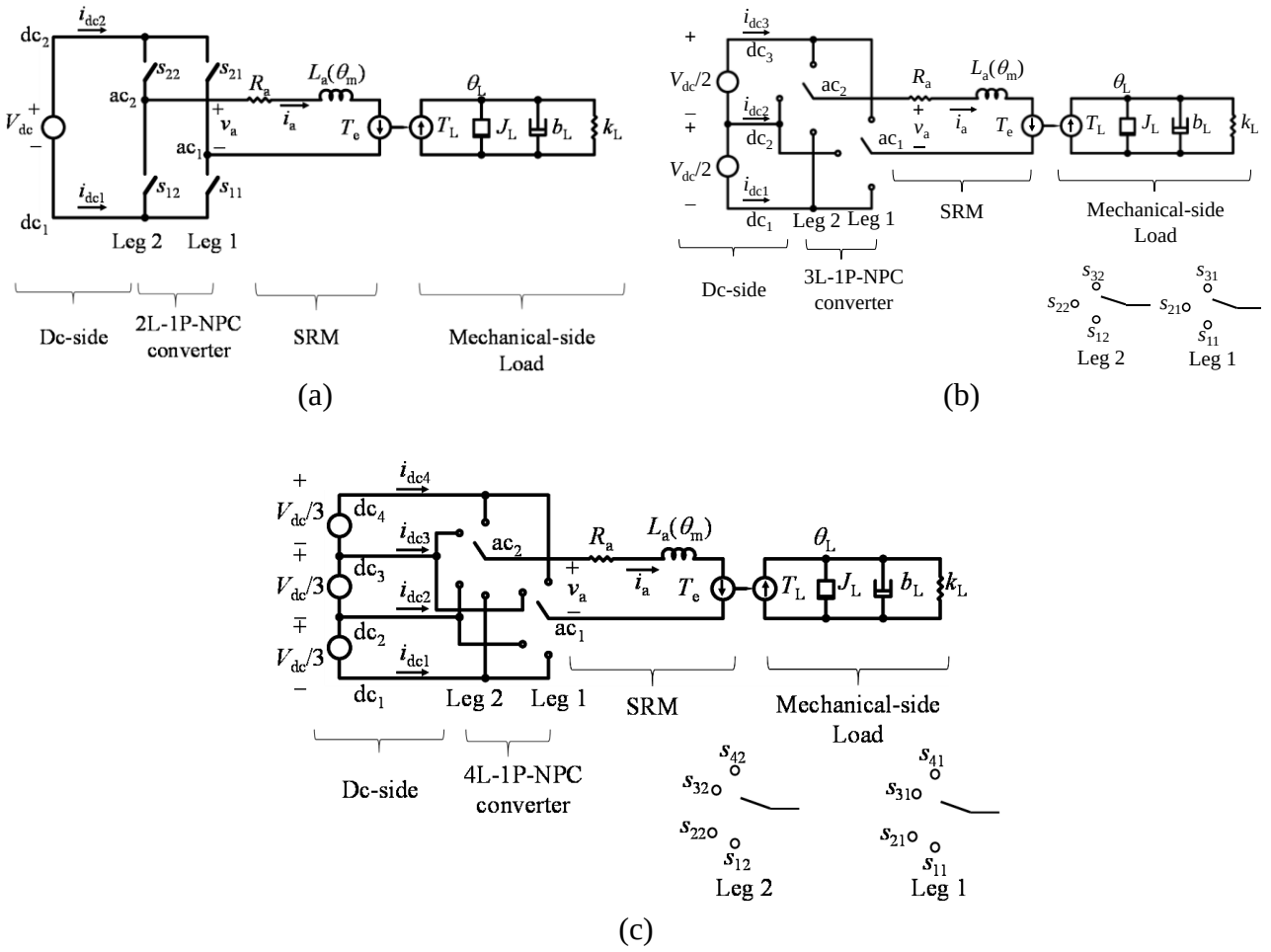


**Figure 1.** Switching models and system architecture for the studied DC–AC converter topologies driving the SPRM–mechanical load system. (a) Topology A: 2L-1P-NPC; (b) Topology B: 3L-1P-NPC; (c) Topology C: 4L-1P-NPC.

Each of the topologies, as depicted in Figure 1, uses a full-bridge configuration of the 1P-NPC converter, which consists of two legs, denoted as Leg 1 and Leg 2. The switching behavior of the converters is governed by switching functions (SFs), denoted as $s_{ij}$, where $i \in \{d_{c1}, d_{c2}, d_{c3}, d_{c4}\}$ and $j \in \{a_{c1}, a_{c2}\}$.

Figure 1(a) presents Topology A, where the SPRM is driven by a 2L-1P-NPC converter. The DC side of this topology is characterized by a single DC voltage source ($v_{dc}(t) \approx V_{dc}$) and two corresponding DC currents ($i_{dc1}(t)$ and $i_{dc2}(t)$).

In Figure 1(b), Topology B is illustrated, showing the SPRM driven by a 3L-1P-NPC converter. In this configuration, the DC side is composed of two equal DC voltage sources, each having a magnitude of $V_{dc}/2$, and the three DC currents ($i_{dcy}(t)$, where $y \in \{1, 2, 3\}$) are specified accordingly.

Finally, Figure 1(c) illustrates Topology C, which features a 4L-1P-NPC converter driving the SPRM. In this topology, the DC side is supplied by three equal DC voltage sources, each having a magnitude of $V_{dc}/3$, and the four DC currents ($i_{dcy}(t)$, where $y \in \{1, 2, 3, 4\}$) are highlighted as part of the system's configuration.

## 3. Modeling the system

In this subsection, the mathematical models for the SPRM and the 1P-NPC converter are developed.

### *3.1. SPRM modeling*

Referring to Figure 1, by applying Kirchhoff's voltage law to the SPRM, its dynamic equation is derived as follows:

$$\frac{\mathrm{d}\lambda_a\left(t,\theta_m(t)\right)}{\mathrm{d}t} = v_a(t) - R_a \cdot i_a(t) \tag{1}$$

where $\lambda_a(t, \theta_m(t))$ represents the concatenated magnetic flux, which is a function of both the time $t$ and the rotor's angular position $\theta_m(t)$. Additionally, it is known that $L_a(t) = \lambda_a(t, \theta_m(t))/i_a(t)$ [17], and by substituting this into (1) and performing algebraic manipulations, the dynamic equation of the electromechanical system is obtained, as shown as follows [17,26]:

$$v_a(t) = R_a \cdot i_a(t) + \omega_m(t) \cdot i_a(t) \cdot \frac{\partial L_a\left(\theta_m(t)\right)}{\partial \theta_m(t)} + L_a\left(\theta_m(t)\right) \cdot \frac{\mathrm{d}i_a(t)}{\mathrm{d}t} \tag{2}$$

Here, $\omega_m(t) = \mathrm{d}\theta_m(t)/\mathrm{d}t$ denotes the angular velocity of the SPRM. By multiplying both sides of (2) by $i_a(t)$, the instantaneous electric power ($p_e(t)$) of the SPRM is obtained, as expressed in:

$$p_e(t) = v_a(t) \cdot i_a(t) = R_a \cdot {i_a}^2(t) + \omega_m(t) \cdot {i_a}^2(t) \cdot \frac{\partial L_s\left(\theta_m(t)\right)}{\partial \theta_m(t)} + L_s\left(\theta_m(t)\right) \cdot i_a(t) \cdot \frac{\mathrm{d}i_a(t)}{\mathrm{d}t} \tag{3}$$

The magnetic energy stored in the inductance $L_a(\theta_m(t))$ is given by $w_g(t) = 0.5 \cdot L_a(\theta_m(t)) \cdot i_a(t)^2$. Hence, the instantaneous rate of change of magnetic energy is given by:

$$\frac{\mathrm{d}w_g(t)}{\mathrm{d}t} = 0.5 \cdot \left[ i_a^2(t) \cdot \omega_m(t) \cdot \frac{\partial L_a\left(\theta_m(t)\right)}{\partial \theta_m(t)} + 2 \cdot i_a(t) \cdot L_a\left(\theta_m(t)\right) \cdot \frac{\mathrm{d}i_a(t)}{\mathrm{d}t} \right] \tag{4}$$

According to Figure 1, the power balance of the electromechanical system can be expressed as $p_e(t) = p_m(t) + p_R(t) + \mathrm{d}w_g(t)/\mathrm{d}t$, where $p_R(t) = R_a \cdot {i_a}^2(t)$ is the power dissipated by the resistance $R_a$, and $p_m(t)$ represents the instantaneous power developed by the mechanical load. Consequently, from the power balance equation, the mechanical power $p_m(t)$ is defined by:

$$p_m(t) = 0.5 \cdot \omega_m(t) \cdot {i_a}^2(t) \cdot \frac{\partial L_a\left(\theta_m(t)\right)}{\partial \theta_m(t)} \tag{5}$$

As it is known, $p_m(t) = T_e(t) \cdot \omega_m(t)$, where $T_e(t)$ is the electromagnetic torque developed by the SPRM, expressed as follows [17,26]:

$$T_{\mathrm{e}}(t) = 0.5 \cdot {i_{\mathrm{a}}}^{2}(t) \cdot \frac{\partial L_{\mathrm{a}}\left(\theta_{\mathrm{m}}(t)\right)}{\partial \theta_{\mathrm{m}}(t)} \tag{6}$$

According to [17] and the application of the two-reaction theory [28], the inductance $L_{\mathrm{a}}(\theta_{\mathrm{m}}(t))$ is defined as follows:

$$L_{\mathrm{a}}\left(\theta_{\mathrm{m}}(t)\right) = 0.5 \cdot \left(\left(L_{\mathrm{a_d}} + L_{\mathrm{a_q}}\right) + \left(L_{\mathrm{a_d}} - L_{\mathrm{a_q}}\right) \cdot \cos\left(2 \cdot \theta_{\mathrm{m}}(t)\right)\right) \tag{7}$$

where $L_{\mathrm{ad}}$ and $L_{\mathrm{aq}}$ represent the inductance along the direct and quadrature axes of the magnetomotive distribution in the SPRM, respectively [17,26,28]. Substituting (7) into (2) and (6) yields the dynamic model of the SPRM, which is given by:

$$\begin{cases} \dfrac{\mathrm{d}i_{\mathrm{a}}(t)}{\mathrm{d}t} = 2 \cdot \dfrac{v_{\mathrm{a}}(t) - R_{\mathrm{a}} \cdot i_{\mathrm{a}}(t)}{L_{\mathrm{a_d}} + L_{\mathrm{a_q}} + \left(L_{\mathrm{a_d}} - L_{\mathrm{a_q}}\right) \cdot \cos\left(2 \cdot \theta_{\mathrm{m}}(t)\right)} + \\ \quad + \dfrac{\left(L_{\mathrm{a_d}} - L_{\mathrm{a_q}}\right) \cdot \omega_{\mathrm{m}}(t) \cdot i_{\mathrm{a}}(t) \cdot \sin\left(2 \cdot \theta_{\mathrm{m}}(t)\right)}{L_{\mathrm{a_d}} + L_{\mathrm{a_q}} + \left(L_{\mathrm{a_d}} - L_{\mathrm{a_q}}\right) \cdot \cos\left(2 \cdot \theta_{\mathrm{m}}(t)\right)} \\ \dfrac{\mathrm{d}\theta_{\mathrm{m}}(t)}{\mathrm{d}t} = \omega_{\mathrm{m}}(t) \\ T_{\mathrm{e}}(t) = -\left(L_{\mathrm{a_d}} - L_{\mathrm{a_q}}\right) \cdot {i_{\mathrm{a}}}^{2}(t) \cdot \sin\left(2 \cdot \theta_{\mathrm{m}}(t)\right) \end{cases} \tag{8}$$

### *3.2. Modeling mechanical load*

The mechanical load, as depicted in Figure 1, is represented by a mechanical network, with its dynamic equation defined as shown in [27]:

$$T_{\mathrm{L}}(t) = J_{\mathrm{L}} \cdot \frac{\mathrm{d}^2\theta_{\mathrm{L}}(t)}{\mathrm{d}t^2} + \mathrm{b}_{L} \cdot \frac{\mathrm{d}\theta_{\mathrm{L}}(t)}{\mathrm{d}t} + k_{\mathrm{L}} \cdot \theta_{\mathrm{L}}(t) \tag{9}$$

Here, $T_{\mathrm{L}}(t)$ is the developed torque, $J_{\mathrm{L}}$ is the moment of inertia, $b_{\mathrm{L}}$ is the damping coefficient, and $k_{\mathrm{L}}$ is the stiffness coefficient of the mechanical load. Assuming a lossless system with no coupling losses between the SPRM rotor and the mechanical load, it follows that $T_{\mathrm{e}}(t) = T_{\mathrm{L}}(t)$.

### *3.3. Modeling the nL-1P-NPC converter*

Referring to Figure 1 and according to [29], the SFs for the *n*L−1P−NPC converter (where $n \in \{1, 2, 3, 4\}$) are defined by:

$$s_{xy}(t) = \begin{cases} 1, & \text{if } x \text{ is connected to } y \\ 0, & \text{else} \end{cases}$$

$$\sum_{x=1}^{n} s_{xy}\,(t) = 1 \tag{10}$$

$$y \in [1, 2]$$

According to (10), the SFs for each leg of the *n*L−1P−NPC converter cannot simultaneously take the value of one, meaning that both switches in a given leg cannot be closed at the same time. Furthermore, the operation of the switches is restricted such that only one switch can be closed at any

given moment [30,31].

In the specific case of the 2L-1P-NPC converter, depicted in Figure 1(a), the voltage $v_a(t)$ and the currents $i_{dc1}(t)$ and $i_{dc2}(t)$ are defined as follows in (11) and (12), respectively [29].

For the multilevel converters ($n$L−1P−NPC), the generalized switching model at $n$ levels is expressed as follows in (13) and (14).

$$v_{\mathrm{a}}(t) = \left(s_{22}(t) - s_{21}(t)\right) \cdot V_{\mathrm{dc}} \tag{11}$$

$$\begin{cases} i_{\mathrm{dc}_1}(t) = \left(s_{12}(t) - s_{11}(t)\right) \cdot i_{\mathrm{a}}(t) \\ i_{\mathrm{dc}_2}(t) = \left(s_{22}(t) - s_{21}(t)\right) \cdot i_{\mathrm{a}}(t) \end{cases} \tag{12}$$

$$v_a(t) = \left(s_{n2}(t) - s_{n1}(t)\right) \cdot V_{dc} + \frac{V_{dc}}{n-1} \cdot \sum_{j=1}^{n-1} j \cdot \left(s_{(j+1)2}(t) - s_{(j+1)1}(t)\right) \tag{13}$$

$$\begin{bmatrix} i_{dc_1}(t) \\ \vdots \\ i_{dc_n}(t) \end{bmatrix} = \begin{bmatrix} s_{12}(t) - s_{11}(t) \\ \vdots \\ s_{n2}(t) - s_{n1}(t) \end{bmatrix} \cdot i_a(t) \tag{14}$$

The switching models for the systems in Topologies B and C are described by (8)–(10), (13), and (14).

## 4. Modulation

This research introduces four candidate modulation strategies for implementation in the $n$L-1P-NPC topologies, as illustrated in Configurations A–C. For the 2L-1P-NPC converter (Topology A), two modulation techniques are applied: BVPWM and UVPWM. In contrast, for multilevel converters ($z$L-1P-NPC where $z \in \{3, 4\}$), VVPWM and LSPWM are used. The following subsections provide a detailed description of each modulation method.

### *4.1. BVPWM analysis*

BVPWM, as part of the standard modulation techniques, has been extensively analyzed, with several contributions available in the literature [29,32–34]. The SFs of the 2L-1P-NPC converter, denoted as $s_{xy}(t)$, where $\{x, y\} \in \{1, 2\}$, are generated by comparing a high-frequency triangular carrier waveform ($v_c(t)$) with a line-frequency sinusoidal control waveform ($v_m(t)$) [29]. For the application of BVPWM to the 2L-1P-NPC topology (Figure 1(a)), the $v_m(t)$ and $v_c(t)$ waveforms are mathematically defined by:

$$v_{\mathrm{m}}(t) = m \cdot \sin(2 \cdot \pi \cdot f \cdot t) \tag{15}$$

$$v_{\mathrm{c}}(t) = \begin{cases} -4 \cdot \dfrac{t}{T_{\mathrm{s}}} + 1, & 0 \le t < \dfrac{1}{2} \cdot T_{\mathrm{s}} \\ 4 \cdot \dfrac{t}{T_{\mathrm{s}}} - 3, & \dfrac{1}{2} \cdot T_{\mathrm{s}} \le t < T_{\mathrm{s}} \end{cases} \tag{16}$$

Here, $m$, $f$, and $T_s$ represent the modulation index, line frequency, and switching period, respectively.

The SFs ($s_{22}(t)$, $s_{11}(t)$) and ($s_{21}(t)$, $s_{12}(t)$) form two paired combinations. The SFs in each pair toggle between zero and one, ensuring that one SF in the pair always holds a value of one [29]. Specifically, when $v_m(t) > v_c(t)$, the SFs $s_{22}(t)$ and $s_{11}(t)$ take the value of one; otherwise, $s_{21}(t)$ and $s_{12}(t)$ are set to one. Figure 2(a) demonstrates the implementation of BVPWM for the 2L-1P-NPC topology, showing the duty ratios ($d_{21}(t)$ and $d_{22}(t)$) of Legs 1 and 2, along with the synthesized output voltage $v_a(t)$. This implementation employs BVPWM under the conditions $m = 0.8$, $f_s = 10$ kHz, and $V_{dc} = 800$ V.

### *4.2. UVPWM analysis*

Similar to BVPWM, UVPWM has been comprehensively examined in previous studies [29,32–34]. The SFs introduced in the BVPWM analysis are now derived by comparing the triangular waveform $v_c(t)$ (from (16)) with two sinusoidal control signals shifted by 180°: $v_{m1}(t)$ and $v_{m2}(t)$. These signals are defined as follows:

$$\begin{cases} v_{m_1}(t) = m \cdot \sin(2 \cdot \pi \cdot f \cdot t) \\ v_{m_2}(t) = m \cdot \sin(2 \cdot \pi \cdot f \cdot t - \pi) \end{cases} \tag{17}$$

In this modulation scheme, the comparison between $v_{m1}(t)$ and $v_c(t)$ governs the switching of SFs for Leg 1, while the comparison between $v_{m2}(t)$ and $v_c(t)$ controls the SFs for Leg 2 [29]. As in BVPWM, when $v_{m1}(t) > v_c(t)$, the SFs $s_{21}(t)$ and $s_{11}(t)$ take the values one and zero, respectively, and vice versa. Similarly, if $v_{m2}(t) > v_c(t)$, the SFs $s_{22}(t)$ and $s_{12(}t)$ take the values one and zero.

Figure 2(b) depicts the UVPWM implementation in the 2L-1P-NPC converter, including the duty ratios ($d_{21}(t)$ and $d_{22}(t)$) of Legs 1 and 2, and the synthesized output voltage $v_a(t)$. The implementation is shown for $m = 0.8$, $f_s = 10$ kHz, and $V_{dc} = 800$ V.

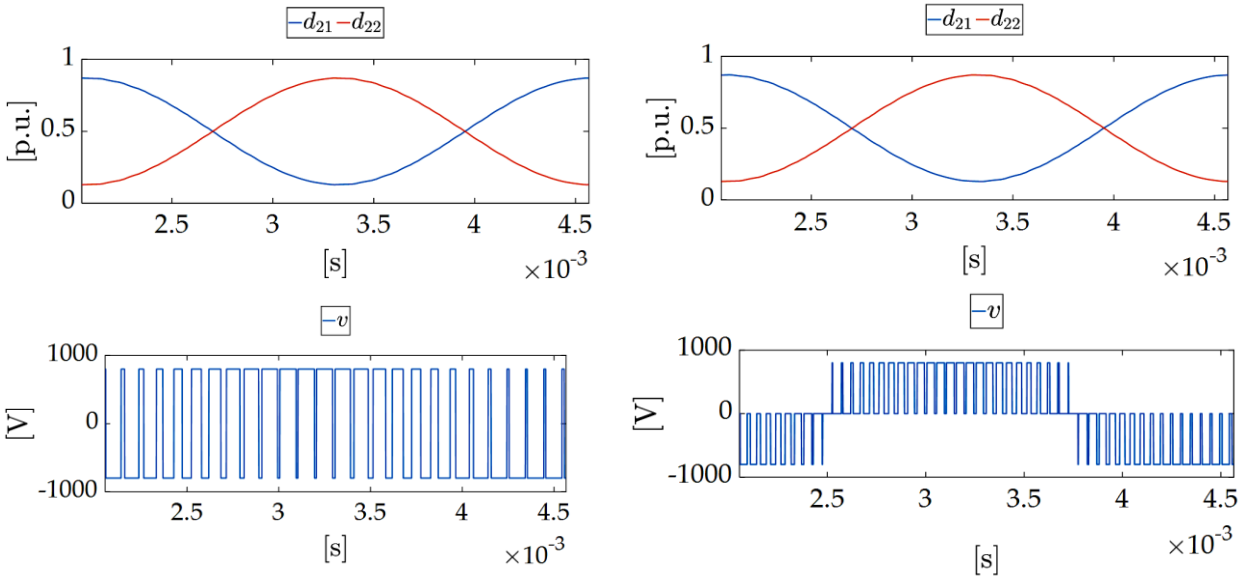


**Figure 2.** Implementation of the BVPWM and UVPWM modulation techniques in the 2L-1P-NPC topology. The modulation is configured with $m = 0.8$, $f_s = 10$ kHz, and $V_{dc} = 800$ V. The figure illustrates the duty ratios $d_{21}$(t) and $d_{22}$(t) for Legs 1 and 2, along with the corresponding output voltage waveform $v_a$(t). (a) BVPWM modulation. (b) UVPWM modulation.

For multilevel converters (zL-1P-NPC, $z \in \{3, 4\}$), two candidate modulations are presented: VVPWM and ($n$−1)-LSPWM. These strategies are described in the following sections, followed by an analysis of their performance in Topologies B and C.

### *4.3. VVPWM analysis*

VVPWM relies on building a special set of space vectors, termed virtual vectors, within the space vector diagram. These vectors are defined as a linear combination of specific switching states [35,36], and each virtual vector ensures a zero average neutral-point current over every switching cycle $T_s$. Thus, synthesizing the reference voltage vector with these virtual vectors maintains balance in the DC-link capacitor voltages in each cycle [35–38]. This modulation strategy can be generalized for $n$-level and $p$-leg converters by using the expressions described below, as introduced in [38].

$$d_x\big(\theta(t)\big) = \frac{m}{NF}\cdot\cos\left(\theta(t)-(x-1)\cdot\frac{2\cdot\pi}{p}\right), \quad x = 1, 2, \cdots, p$$

$$\begin{cases} \text{Even } p: NF = 1 \\ \text{Odd } p: NF = \cos\left(\frac{1}{2}\cdot\frac{\pi}{p}\right) \end{cases} \tag{18}$$

$$\begin{cases} d_{x,1}\big(\theta(t)\big) = \dfrac{1}{2}\cdot\Big(\max\big[d_1\big(\theta(t)\big), d_2\big(\theta(t)\big), \cdots, d_p(\theta)(t)\big]\Big) - d_x\big(\theta(t)\big) \\ d_{x,n}\big(\theta(t)\big) = \dfrac{1}{2}\cdot\Big(d_x\big(\theta(t)\big) - \min\big[d_1\big(\theta(t)\big), d_2\big(\theta(t)\big), \cdots, d_p(\theta)\big]\Big) \\ d_{x,y}(\theta) = \dfrac{1}{n-2}\cdot\Big(1 - d_{x,1}(\theta) - d_{x,n}(\theta)\Big) \\ x = 1, 2, \cdots, p;\ y = 2, 3, \cdots, n-1 \end{cases} \tag{19}$$

The modulation waveforms $d_x(\theta(t))$ for each converter leg are given by (18), where $\theta(t) = \omega\cdot t$, $m$ is the modulation index, and $NF$ is the normalization factor to maintain $m$ within the [0, 1] linear modulation range [38]. Since the converter is configured as a full bridge (two legs), $p$ is set to 2.

The duty ratios for the connection of the AC-side and DC-side rails (denoted as $d_{x,y}$) are determined using (19), combined with a symmetrical staircase-type distribution over one $T_s$. Figure 3 illustrates the duty ratio pattern for $n$ =3, $p$ = 2, and $m$ = 0.80.

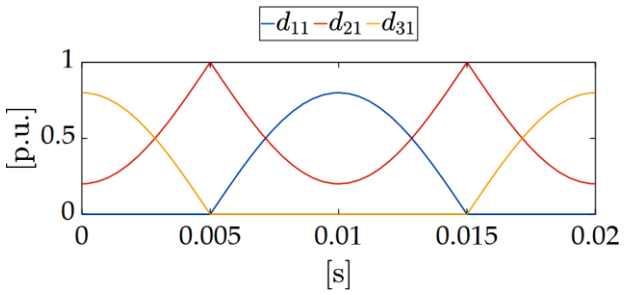


**Figure 3.** Leg duty ratio distribution for the selected pulsewidth modulation (PWM) strategy in a multilevel converter. The pattern is shown for $n$ = 3, $p$ = 2, and $m$ = 0.80, illustrating the modulation behavior and switching sequences within the converter topology.

### *4.4. LSPWM analysis*

LSPWM has been thoroughly explored in the literature [39–43]. This method compares a modulating waveform, typically sinusoidal, with $n$–1 carrier signals, each corresponding to a voltage level. When the modulating signal exceeds a given carrier, the associated voltage level is generated [42]. A potential implementation is depicted in Figure 4(a), and the duty ratio pattern for $n$ = 3 is shown in Figure 4(b). The modulating waveform is defined by $v_m(t) = V_m \cdot \sin(2 \cdot \pi \cdot f_m \cdot t)$, where $V_m$ and $f_m$ are the peak amplitude and frequency (with $f_m$ = 50 Hz).

The following expression:

$$v_{carr}(t) = 2 \cdot V_{carr} \cdot f_s \cdot \left( \frac{1}{2} \cdot \frac{1}{f_s} - \text{abs}\left( \left(t + \phi_{carr}(t)\right) \cdot \text{mod}\left(\frac{1}{f_s}\right) - \frac{1}{2} \cdot \frac{1}{f_s} \right) \right) + \frac{n-1-k}{k} \tag{20}$$

defines the carriers, where $V_{carr}$, $\phi_c$, and $f_s$ are the carrier amplitude, phase angle, and switching frequency, respectively [43]. Comparisons between the modulating signal and the carriers are defined as follows:

$$\begin{cases} v_m(t) > v_{carr}(i-2,k), i > k+1, \text{where } i_\alpha \\ v_m(t) < v_{carr}(i-1,k), i < k+1, \text{where } i_\beta \end{cases} \tag{21}$$

From here, $i_\alpha = k + 2, k + 3, \ldots, 2 \cdot k + 1$ and $i_\beta = 1, 2, \ldots, k$.

## 5. Thermal analysis of two-level and multilevel converters for single-phase reluctance motor drives

Thermal performance is a critical factor influencing the efficiency, reliability, and lifespan of power converters. In electric motor drive applications, excessive heat generation in power semiconductor devices, passive components, and interconnection elements can degrade the system's performance and lead to failure mechanisms such as bond wire fatigue, solder joint cracking, and thermal runaway [44,45].

Multilevel converters offer a significant advantage over conventional two-level topologies by distributing the voltage stress across multiple switching devices, thereby reducing switching losses and improving harmonic performance. However, the increased number of components in higher-level converters introduces additional conduction losses, making thermal optimization crucial. This section provides a comprehensive analysis of power losses and thermal behavior in 2L-1P-NPC, 3L-1P-NPC, and 4L-1P-NPC converters, evaluating their impact on the system's thermal performance [44,45].

### *5.1. Power loss estimation in power semiconductors*

The total power dissipation in a converter comprises switching losses, conduction losses, and passive component losses. The total power loss ($P_{total}$) is given by [29]:

$$P_{total} = P_{sw} + P_{cond} + P_{core} + P_{copper} \tag{22}$$

where $P_{sw}$, $P_{cond}$, $P_{core}$, and $P_{copper}$ are the switching losses in power semiconductor devices, the conduction losses in the switches, the magnetic core losses in inductors, and the copper (winding) losses in the inductors and transformer, respectively.

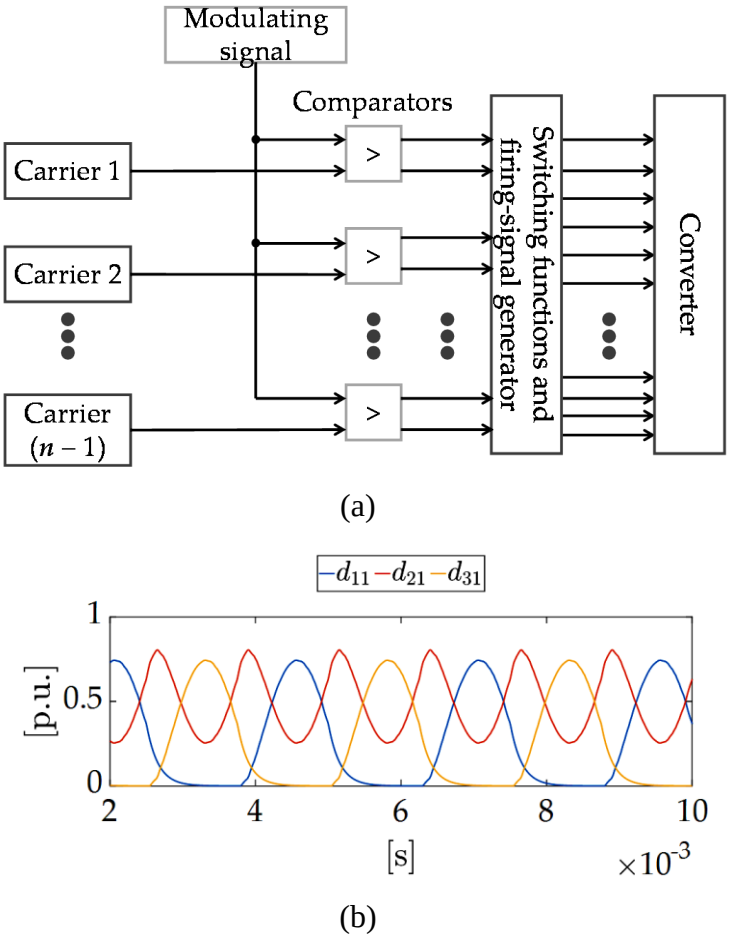


**Figure 4.** Implementation of LSPWM and duty ratio distribution in a multilevel converter. (a) Diagram illustrating the LSPWM scheme, where $(n - 1)$ carrier signals are compared with the modulating signal [43]. (b) Leg duty ratio pattern for LSPWM, shown for $n = 3$.

Conduction losses occur when the power semiconductor devices are in the on state. The conduction loss per switch is calculated as follows:

$$P_{cond} = I_{rms}^{2} \cdot R_{on} \tag{23}$$

In this context, $I_{rms}$ and $R_{on}$ are the rms current through the switch and the on-state resistance of the semiconductor device [29].

For multilevel converters, the voltage stress per switch is reduced, leading to lower conduction losses per device. However, the increased number of switches in three- and four-level converters contributes to additional conduction loss [22].

Switching losses occur during the transition between the on and off states due to the overlap of voltage and current waveforms. The loss per switch is given by [22,29]:

$$P_{sw} = 0.5 \cdot V_{dc} \cdot I_{load} \cdot (t_{on} + t_{off}) \cdot f_{sw} \tag{24}$$

Here, $V_{dc}$ and $I_{load}$ are the DC-link voltage and the load current, respectively. Moreover, $t_{on}$, $t_{off}$, and $f_{sw}$ are the turn-on and turn-off times and the switching frequency, respectively.

Multilevel converters exhibit lower voltage steps per switching event, significantly reducing $P_{sw}$

compared with a two-level topology. However, the total number of switching transitions increases, which may counteract this benefit in higher-level converters [22].

### *5.2. Power losses in passive components*

In addition to semiconductor losses, inductors and transformers in converters also contribute to thermal stress through core losses and copper losses [44,45].

Core losses in magnetic components arise due to hysteresis and eddy currents. These losses are estimated using Steinmetz's equation [46]:

$$P_{sw} = k \cdot f_{sw}^{\alpha} \cdot B_{max}^{\beta} \cdot V_{core} \tag{25}$$

where $k$ is the material-dependent constant, and $f_{sw}$, $B_{max}$, and $V_{core}$ are the switching frequency and the maximum flux density, and the core volume, respectively. Finally, $\alpha$ and $\beta$ are empirical coefficients for the material.

Higher-level converters exhibit lower peak inductor currents, which can reduce core losses by decreasing $B_{max}$. However, the increased number of inductors in multilevel topologies may introduce additional thermal constraints [22].

On the other hand, copper losses in inductors and transformers are given by:

$$P_{copper} = I_{rms}^{2} \cdot R_{winding} \tag{26}$$

where $R_{winding}$ is the winding resistance. Multilevel converters typically reduce $I_{rms}$, thereby lowering copper losses.

### *5.3. Junction temperature and thermal resistance modeling*

The temperature rise in power semiconductors is governed by their thermal resistance network. The junction temperature ($T_j$) is estimated as [47] indicated in:

$$T_j = P_{total} \cdot R_{th\text{-}jc} + T_c \tag{27}$$

Here, $R_{th\text{-}jc}$ and $T_c$ are the thermal resistance from the junction to the case and the case temperature, respectively. Also, $R_{th\text{-}jc} + R_{th\text{-}ca}$ is the case-to-ambient resistance.

Higher-level converters typically experience lower switching losses and lower junction temperature, but the total conduction losses increase due to the additional semiconductor devices [22].

## 6. Control system

The system configurations depicted in Topologies A–C operate as a servomechanism with velocity feedback, where the primary control goal is to regulate the angular velocity of the mechanical load by controlling the angular position of the SPRM, denoted as $\theta_m(t)$ [48]. Figure 5 illustrates a control scheme applicable to all the topologies under consideration. An open-loop control strategy is employed to regulate $v_a(t)$ using the $n$L−1P−NPC converter (where $n \in \{2, 3, 4\}$). In this approach, a constant modulation index $m$ is selected, and the switching states ($s_{zx}(t) \in \{1, 2, 3, 4\}$ and $x \in \{1, 2\}$) are determined by the modulator according to the chosen modulation technique, such as VBPWM, UVPWM, VVPWM, or LSPWM.

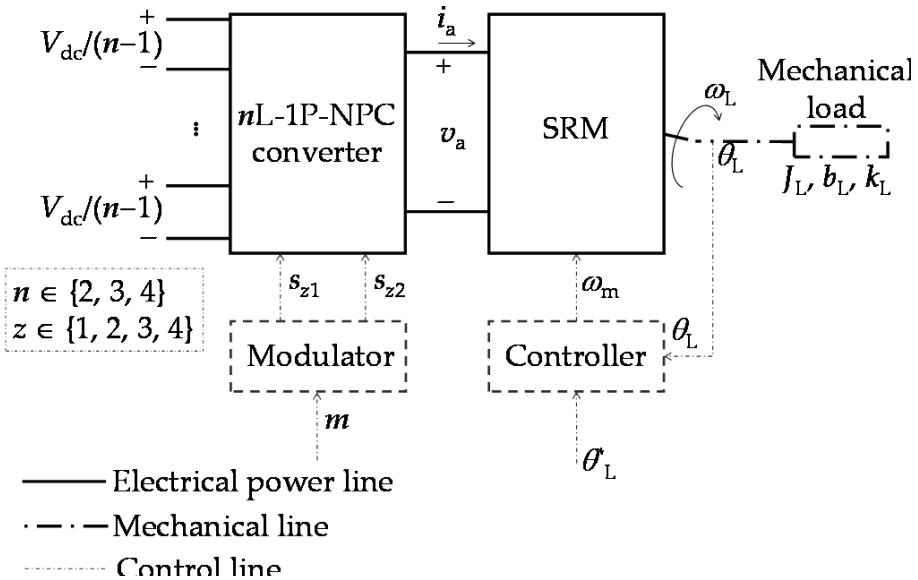


**Figure 5.** Control system architecture for Topologies A–C. The *n*L-1P-NPC converter is cascaded with the SPRM–mechanical load system, illustrating the integration of the power converter, the modulator, and control loops. The diagram highlights both the open-loop control (modulator driven with a constant *m*) and the closed-loop control (PI-based compensator regulating angular position and velocity).

The closed-loop control of the SPRM is executed via a proportional–integral (PI) linear feedback output compensator. The measured variable, specifically the angular position of the mechanical load $\theta_L(t)$, is compared with a reference angular position $\theta_L^*(t)$, generating a position error signal $\theta_L^*(t) - \theta_L(t)$. This error signal is then processed by the PI compensator to produce the controlled variable $\omega_m(t)$, which serves as the control input to the SPRM.

The plant model subjected to control is derived from the linearization of the nonlinear models presented in (8) and (9).

To simplify the explanation, the linearization process is omitted, and the resulting linearized state-space model of the system is given by the following:

$$\begin{cases} \dot{\mathbf{x}}(t) = \mathbf{A} \cdot \mathbf{x}(t) + \mathbf{B} \cdot \mathbf{u}(t) \\ \mathbf{y}(t) = \mathbf{C} \cdot \mathbf{x}(t) + \mathbf{D} \cdot \mathbf{u}(t) \end{cases} \tag{28}$$

where $\mathbf{x}(t) = \left[\hat{\imath}_a(t), \hat{\theta}_m(t), \hat{\theta}_L(t), \hat{\omega}_L(t)\right]^T$, $\mathbf{u}(t) = \left[\hat{v}_a(t), \hat{T}_L(t)\right]^T$, and $\mathbf{y}(t) = \left[\hat{\imath}_a(t), \hat{\theta}_m(t), \hat{\theta}_L(t), \hat{\omega}_L(t), \hat{T}_e(t)\right]^T$ and $\mathbf{x}(t) \in \mathbb{R}^4$, $\mathbf{u}(t)$ $\mathbb{R}^2$, and $\mathbf{y}(t) \in \mathbb{R}^5$ represent the state, input, and output vectors, respectively. The hatted variables correspond to small-signal variables resulting from the linearization [31,48]. The matrices **A**, **B**, **C**, and **D** represent the state, input, output, and direct transmission matrices, respectively, as defined in (29). The constants $K_1$–$K_6$ are set as in (30). Here, the capitalized terms represent the steady-state variables derived from the equilibrium model described in (8) and (9). The steady-state angular velocity is denoted as $\Omega_m$.

$$\mathbf{A} = \begin{bmatrix} K_1 & K_2 & 0 & 0 \\ 0 & 0 & 0 & 1 \\ 0 & 0 & 0 & 1 \\ 0 & 0 & K_3 & K_4 \end{bmatrix}, \ \mathbf{B} = \begin{bmatrix} 1 & 0 \\ 0 & 0 \\ 0 & 0 \\ 0 & 1 \end{bmatrix}$$

$$\mathbf{C} = \begin{bmatrix} 1 & 0 & 0 & 0 \\ 0 & 1 & 0 & 0 \\ 0 & 0 & 1 & 0 \\ 0 & 0 & 0 & 1 \\ K_5 & K_6 & 0 & 0 \end{bmatrix}, \mathbf{D} = \text{zeros (4,2)} \tag{29}$$

$\mathbf{A} \in M_{4x4}$ {K}, $\mathbf{C} \in M_{5x4}$ {K}, and {**B**, **D**} $\in M_{4x2}$ {K}

$$\begin{gathered} K_1 = -2 \cdot \left[ \frac{R_\mathrm{a} - \left(L_{\mathrm{a_d}} - L_{\mathrm{a_q}}\right) \cdot \Omega_\mathrm{m} \cdot \sin(2 \cdot \Theta_\mathrm{m})}{L_{\mathrm{a_d}} + L_{\mathrm{a_q}} + \left(L_{\mathrm{a_d}} - L_{\mathrm{a_q}}\right) \cdot \cos(2 \cdot \Theta_\mathrm{m})} \right] \\ K_2 = 4 \cdot \left[ \frac{(V_\mathrm{a} - R_\mathrm{a} \cdot I_\mathrm{a}) \cdot \left(L_{\mathrm{a_d}} - L_{\mathrm{a_q}}\right) \cdot \sin(2 \cdot \Theta_\mathrm{m})}{L_{\mathrm{a_d}} + L_{\mathrm{a_q}} + \left(L_{\mathrm{a_d}} - L_{\mathrm{a_q}}\right)^2 \cdot \cos(2 \cdot \Theta_\mathrm{m})} \right] \\ K_3 = -\frac{k_\mathrm{L}}{J_\mathrm{L}} \\ K_4 = -\frac{b_\mathrm{L}}{J_\mathrm{L}} \\ K_5 = -2 \cdot \left(L_{\mathrm{a_d}} - L_{\mathrm{a_q}}\right) \cdot I_\mathrm{a} \cdot \sin(2 \cdot \Theta_\mathrm{m}) \\ K_6 = -2 \cdot \left(L_{\mathrm{a_d}} - L_{\mathrm{a_q}}\right) \cdot {I_\mathrm{a}}^2 \cdot \cos(2 \cdot \Theta_\mathrm{m}) \end{gathered} \tag{30}$$

The steady-state conditions for the servomechanism are defined by the cancellation of the time derivatives in (8) and (9), leading to the following equilibrium equations, given by:

$$\begin{cases} V_\mathrm{a} - R_\mathrm{a} = 0 \\ \left(L_{\mathrm{a_d}} - L_{\mathrm{a_q}}\right) \cdot {I_\mathrm{a}}^2 \cdot \sin(2 \cdot \Theta_\mathrm{m}) - k_\mathrm{L} \cdot \Theta_\mathrm{L} = 0 \end{cases} \tag{31}$$

From these equations, the unknowns $I_\mathrm{a}$ and $\Theta_\mathrm{m}$ are solved and expressed as follows:

$$\begin{cases} I_\mathrm{a} = \dfrac{V_\mathrm{a}}{R_\mathrm{a}} \\ \Theta_\mathrm{m} = 0.5 \cdot \sin^{-1}\left( \dfrac{k_\mathrm{L} \cdot {R_\mathrm{a}}^2 \cdot \Theta_\mathrm{L}}{{V_\mathrm{a}}^2 \cdot \left(L_{\mathrm{a_d}} - L_{\mathrm{a_q}}\right)} \right) \end{cases} \tag{32}$$

Finally, by applying the Laplace transform to the linear state-space model in (28), with zero initial conditions, the transfer functions of the system are derived by:

$$\frac{\mathbf{Y}(s)}{\mathbf{U}(s)} = \mathbf{C} \cdot (s \cdot \mathbf{I} - \mathbf{A})^{-1} \cdot \mathbf{B} + \mathbf{D} \tag{33}$$

where $\mathbf{Y}(s) \in \{\mathbb{C}\}^5$, $\mathbf{U}(s) \in \{\mathbb{C}\}^2$, and $\mathbf{I}$ is the identity matrix of 4 x 4 size.

On the basis of this model, the PI controller for the control system is designed, as illustrated in Figure 5.

## 7. Simulation results

The switching models for the converter Topologies A, B, and C were meticulously simulated within the MATLAB-Simulink environment to rigorously analyze the system's performance across diverse operational scenarios. Table 1 details the specific simulation parameters used, including the inductance, resistance, and mechanical properties of the load, ensuring an accurate representation of real-world operating conditions.

All converters—namely, the *n*L-1P-NPC converters, with $n \in \{2, 3, 4\}$—were set to function at a constant switching frequency of $f_s$ = 10 kHz. The initial mechanical load parameters were established with an angular position $\theta_{L0}$ = 0 deg and an angular velocity $\omega_{L0}$ = 0 rad/s. The SPRM was operated at a frequency $f$ = 50 Hz, with a reference angular position $\theta_L^*(t)$ = 30 deg. These reference values were selected to represent an intermediate operating condition that closely reflects industrial applications such as pumps and fans, thereby enabling the generalization of results for real-world performance.

The simulation covered four distinct operating scenarios for each topology. In Scenarios 1 and 2, the 2L-1P-NPC converters utilized the BVPWM and UVPWM modulation schemes, respectively. In Scenarios 3 and 4, the 3L-1P-NPC and 4L-1P-NPC converters operated using the LSPWM and VVPWM modulation techniques.

Figure 6(a,b) exhibit the steady-state responses for the SPRM variables $v_a(t)$, $i_a(t)$, and $T_e(t)$; the 2L-1P-NPC converter states $i_{dc2}(t)$; and the duty cycles $d_{11}(t)$ and $d_{21}(t)$ for Leg 1, along with the mechanical load dynamics $\omega_L(t)$, all corresponding to Scenarios 1 and 2 of Topology A (Figure 1(a)). The analysis confirms that the voltage waveform $v_a(t)$ closely corresponds to the modulation scheme applied. Under Scenario 1 with BVPWM, $v_a(t)$ transitions between $\pm V_{dc}$, while $i_{dc2}(t)$ contains a pronounced 100 Hz sinusoidal component, aligning with twice the SPRM's fundamental operating frequency, as supported by [29]. Conversely, under UVPWM (Scenario 2), $v_a(t)$ oscillates between 0 and $\pm V_{dc}$, and the current $i_{dc2}(t)$ exhibits a "shark-tail" profile with significantly reduced ripple, confirming observations from [29]. Furthermore, the duty cycles $d_{11}(t)$ and $d_{21}(t)$ consistently maintain a 180 °phase shift across both scenarios, a characteristic intrinsic to UVPWM modulation.
Figures 7(a), 8(a), 7(b), and 8(b) depict the steady-state behavior for Topologies B and C (Figure 1(b) and 1(c)), respectively, in Scenarios 3 and 4. For Topology B, the voltage $v_a(t)$ adopts a stepped waveform typical of three-level converters, presenting levels of 0, $\pm V_{dc}/2$, and $\pm V_{dc}$ for both LSPWM and VVPWM [22]. The duty cycles $d_{11}(t)$, $d_{21}(t)$, and $d_{31}(t)$ maintain their characteristic phase shifts, contributing to more refined voltage synthesis. In Topology C, the four-level converter introduces additional voltage steps, achieving values of 0, $\pm V_{dc}/3$, $\pm 2 \cdot V_{dc}/3$, and $V_{dc}$. The duty cycle $d_{21}(t)$ demonstrates saturation in Scenario 3 but operates equivalently to $d_{31}(t)$ in Scenario 4 [22].

**Table 1.** Simulation parameters used for system modeling and analysis. This table presents the key electrical and mechanical parameters, including the inductance, resistance, load properties, and operating conditions for the SPRM-driven multilevel converter system.

| Parameter | Value | Parameter | Value |
|---|---|---|---|
| $L_{ad}$ | 20 (mH) | $b_L$ | 6 (Nms/rad$^2$) |
| $L_{aq}$ | 10 (mH) | $k_L$ | 139 (Nm/rad$^2$) |
| $R_a$ | 0.8 (Ω) | $m$ | 0.85 |
| $J_L$ | 0.7 (kg/m$^2$) | $V_{dc}$ | 800 (V) |

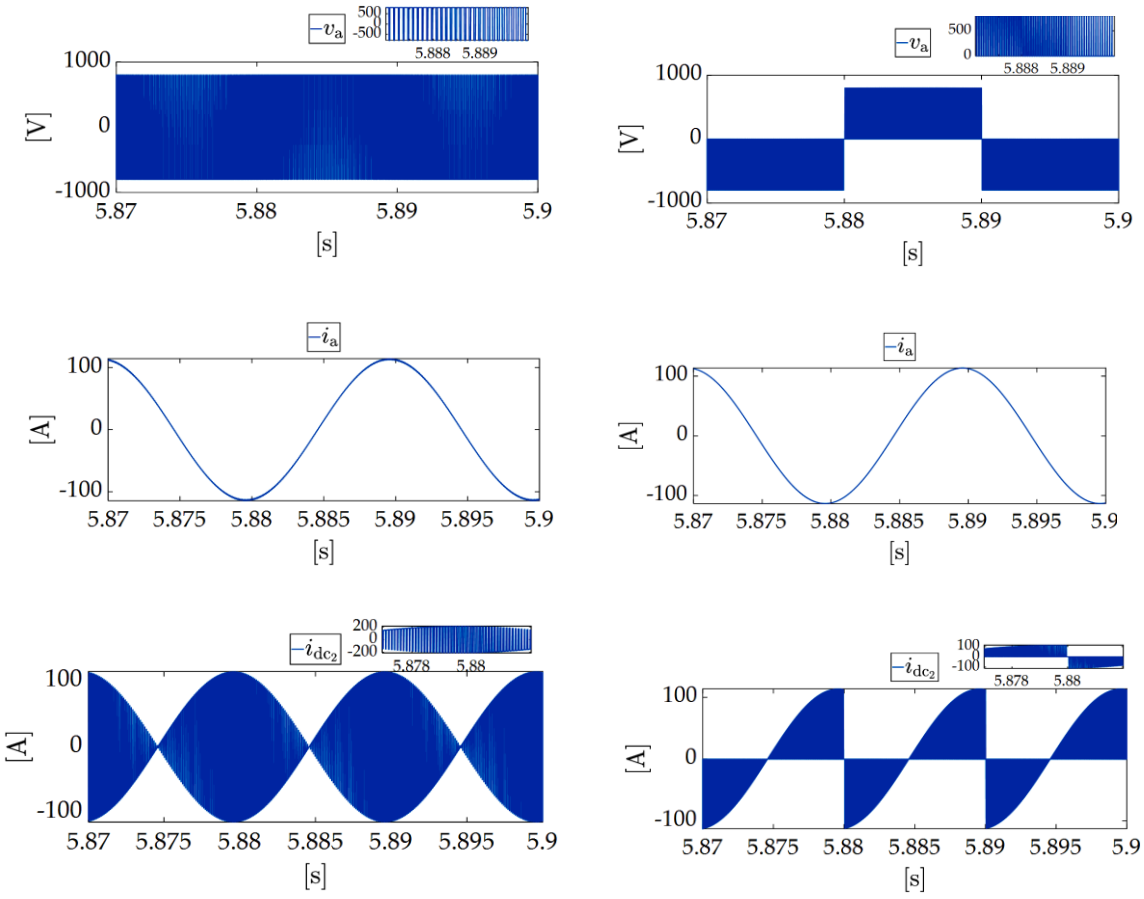


(a) (b)

**Figure 6.** Steady-state simulation results for Topology A (2L-1P-NPC). The system operates under steady-state conditions, with an initial mechanical load position of $\theta_{L0} = 0°$ and an angular velocity $\omega_{L0} = 0$ rad/s. The figure illustrates the converter's dynamics, including the DC-side current $i_{dc2}(t)$ and duty ratios $d_{11}(t)$ and $d_{12}(t)$ for Leg 1, as well as the SPRM electrical variables $v_a(t)$, $i_a(t)$, and electromagnetic torque $T_e(t)$. The mechanical response $\omega_L(t)$ is also depicted. (a) Scenario 1. (b) Scenario 2.

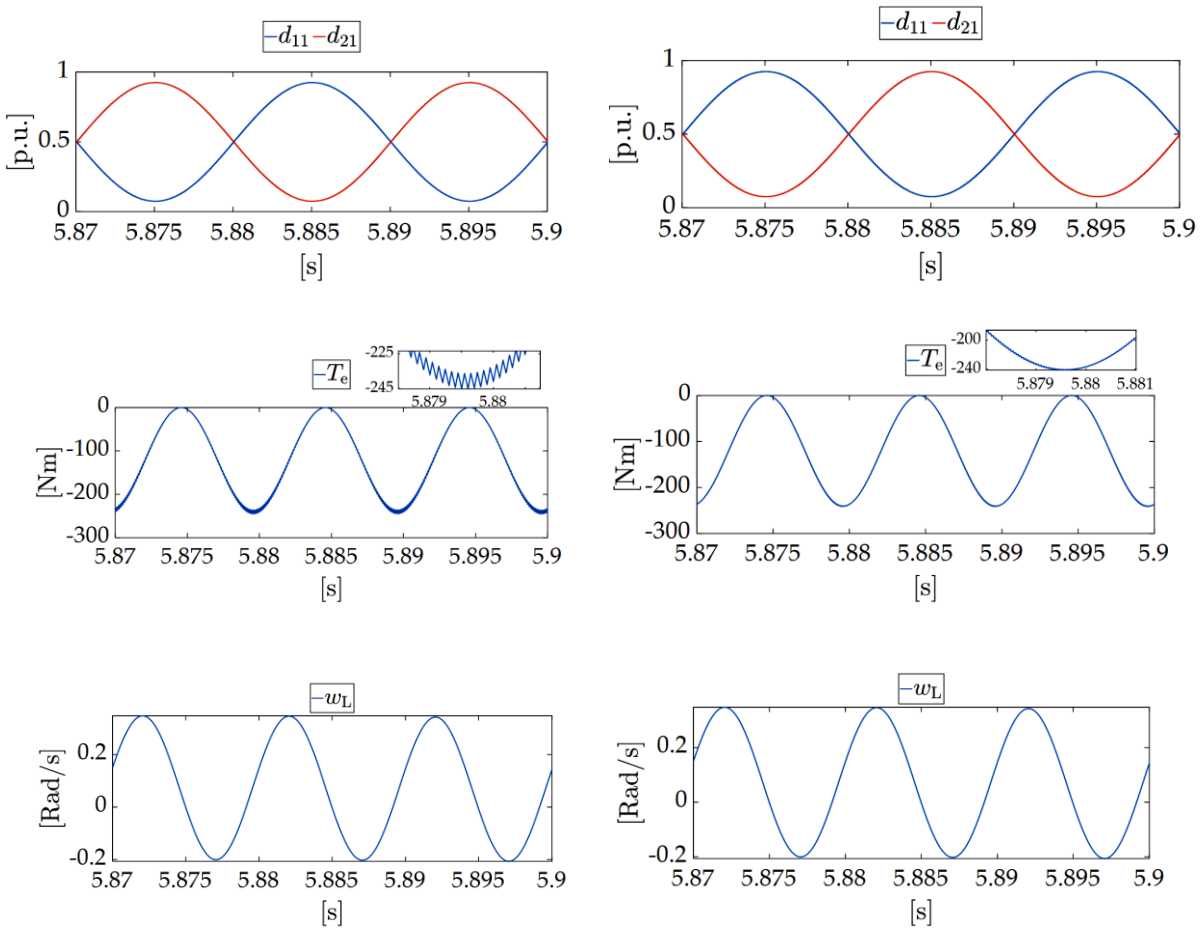


**Figure 6.** Continued.

The electromagnetic torque $T_e(t)$, a critical factor for mechanical performance, showed an approximate ripple of 8.8 Nm in Topology A under BVPWM (Figure 6(a)), which was virtually eliminated when UVPWM was employed (Figure 6(b)). In Scenarios 3 and 4, the torque ripple remained negligible, confirming the efficiency of higher-level converters [22]. Additionally, the analysis of the duty cycles revealed that the shifts in $d_{11}(t)$, $d_{21}(t)$, $d_{31}(t)$, and $d_{41}(t)$ have a direct impact on the harmonic profile and torque characteristics. The THD analysis presented in Table 2 substantiates the claim that multilevel converters offer superior harmonic performance. Topology A exhibited the highest THD for $v_a(t)$ at 133% under BVPWM, whereas the lowest THD was observed in Topology C with LSPWM, registering at 23.66%.

These findings are in congruence with [29], emphasizing that UVPWM effectively reduces THD in two-level NPC converters. As the converter levels increased, the waveform of $v_a(t)$ approached an ideal sinusoidal form, minimizing THD and enhancing the system's overall performance. Regarding $T_e(t)$, THD consistently remained below 2% across all scenarios, with the highest value observed in Scenario 1 of Topology A, corroborating the theoretical expectations [23,49]. The significance of the THD reduction lies in its direct impact on the system's performance, specifically, minimizing torque ripple, enhancing operational smoothness, and reducing acoustic noise and mechanical wear.

To further validate the dynamic characteristics of the converter topologies, Figure 9 presents the transient response of the system under step changes in the load's angular position $\theta_L(t)$ and angular velocity $\omega_L(t)$, considering Topologies A, B, and C for Scenarios 2 and 4. In Figure 9(a), the system is configured as Topology A in Scenario 2, while Figure 9(b,c) illustrates the dynamics for Topologies B and C in Scenario 4. Initially, $\theta_L^*(t) = 30\,°$ and at $t = 4$ s, the step change increases $\theta_L^*(t)$ to 80 °, followed by another step change to $\theta_L^*(t) = 50\,°$ at $t = 10$ s. Across all scenarios, the system exhibits negligible steady-state errors in $\theta_L(t)$, and the velocity $\omega_L(t)$ responds appropriately to step changes, demonstrating relative stability and minimal overshoot [48,50].

To enhance the clarity of the transient performance comparison, the key metrics—rise time, settling time, overshoot, and steady-state error—have been extracted from Figure 9 and summarized in Table 3. As shown, Topology C provides the fastest response with the lowest overshoot and error, followed by Topology B, and finally Topology A. This demonstrates that higher-level converters not only reduce harmonic distortion but also significantly improve the dynamic control behavior, which is essential in high-precision motion applications.

**Table 2.** THD analysis of output voltage $v_a(t)$ and electromagnetic torque $T_e(t)$ across different converter topologies and modulation schemes. This table quantifies the impact of converter levels and modulation techniques on harmonic distortion, highlighting the effectiveness of higher-level topologies in reducing THD and improving the system's performance.

| Variable | Converter level | Modulation | THD (%) |
|---|---|---|---|
| $v_a(t)$ | 2 | BVPWM | 133.00 |
| | | UVPWM | 70.57 |
| | 3 | LSPWM | 38.37 |
| | | VVPWM | 38.38 |
| | 4 | LSPWM | 23.66 |
| | | VVPWM | 36.07 |
| $T_e(t)$ | 2 | BVPWM | 1.80 |
| | | UVPWM | 0.42 |
| | 3 | LSPWM | 0.21 |
| | | VVPWM | 0.21 |
| | 4 | LSPWM | 0.17 |
| | | VVPWM | 0.17 |

**Table 3.** Quantitative transient performance metrics for $\theta_L(t)$ (extracted from Figure 9).

| Topology | Rise time (s) | Settling time (s) | Overshoot (%) | Steady-state error |
|---|---|---|---|---|
| **2L-1P-NPC** | 0.42 | 0.56 | 5.6 | 0.8 |
| **3L-1P-NPC** | 0.31 | 0.41 | 0.41 | 0.4 |
| **4L-1P-NPC** | 0.24 | 0.28 | 0.28 | 0.1 |

In regard to the thermal analysis associated with each topology, the estimation of the total power dissipated is conducted, as expressed in (22). In order to obtain the variables and constants, and consequently calculate a given operating point, certain values were assumed according to [51,52], which are enumerated in Table 4. In order to evaluate the power losses and thermal losses, all the calculation models established in (22)−(27) have been considered. According to the values listed in Table 4, all these losses are calculated according to the topology studied in Table 5; this calculation is summarized in Table 5.

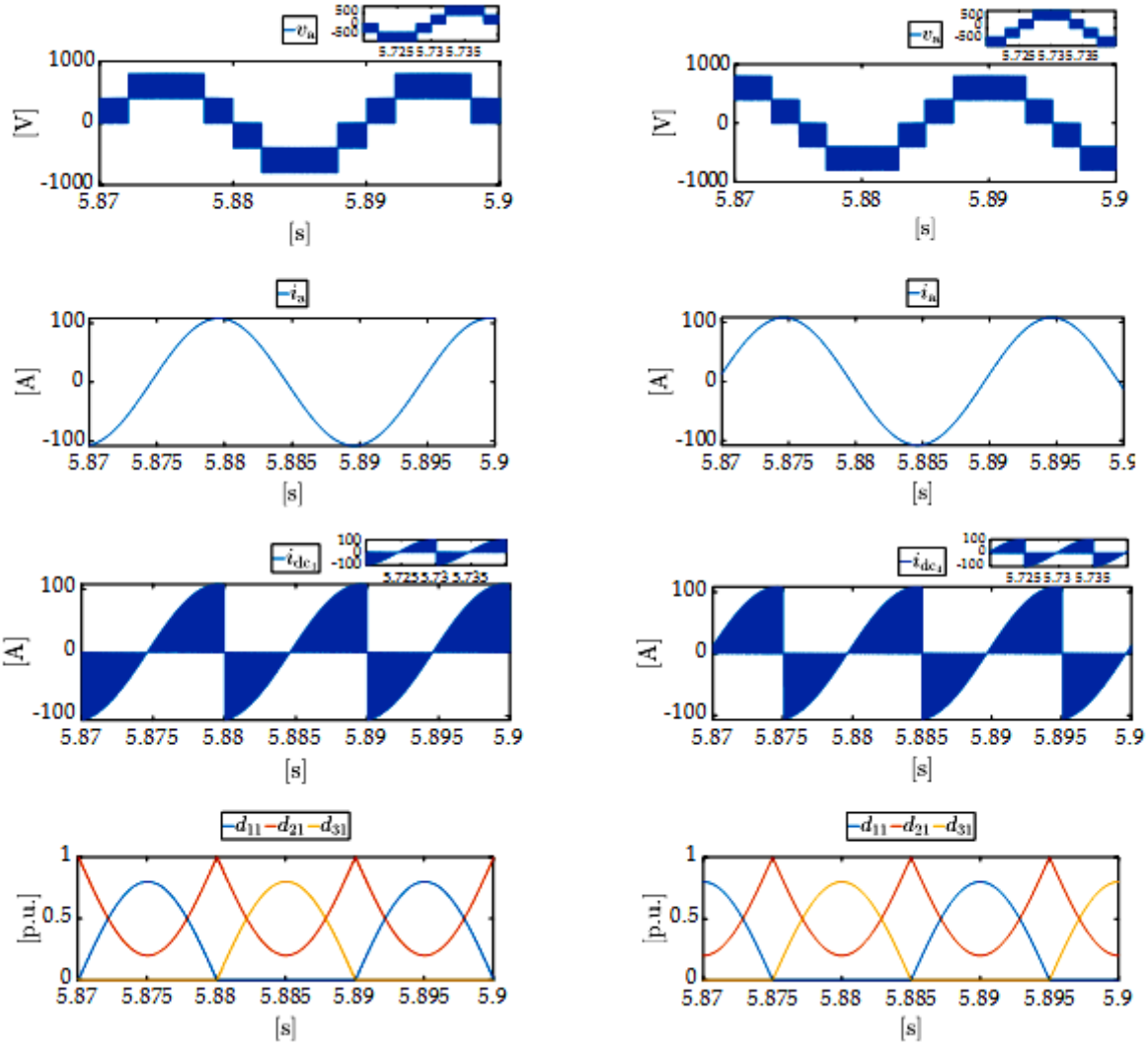


**Figure 7.** Steady-state simulation results for Topology A (2L-1P-NPC) under different modulation scenarios. The system is initialized with a mechanical load position of $\theta_{L0} = 0°$ and an angular velocity of $\omega_{L0} = 0$ rad/s. The figure presents the converter dynamics, including DC-side current $i_{dc2}(t)$ and duty ratios $d_{11}(t)$ and $d_{12}(t)$ for Leg 1, alongside the SPRM electrical variables $v_a(t)$, $i_a(t)$, and electromagnetic torque $T_e(t)$. The mechanical response $\omega_L(t)$ is also illustrated. (a) Scenario 1. (b) Scenario 2.

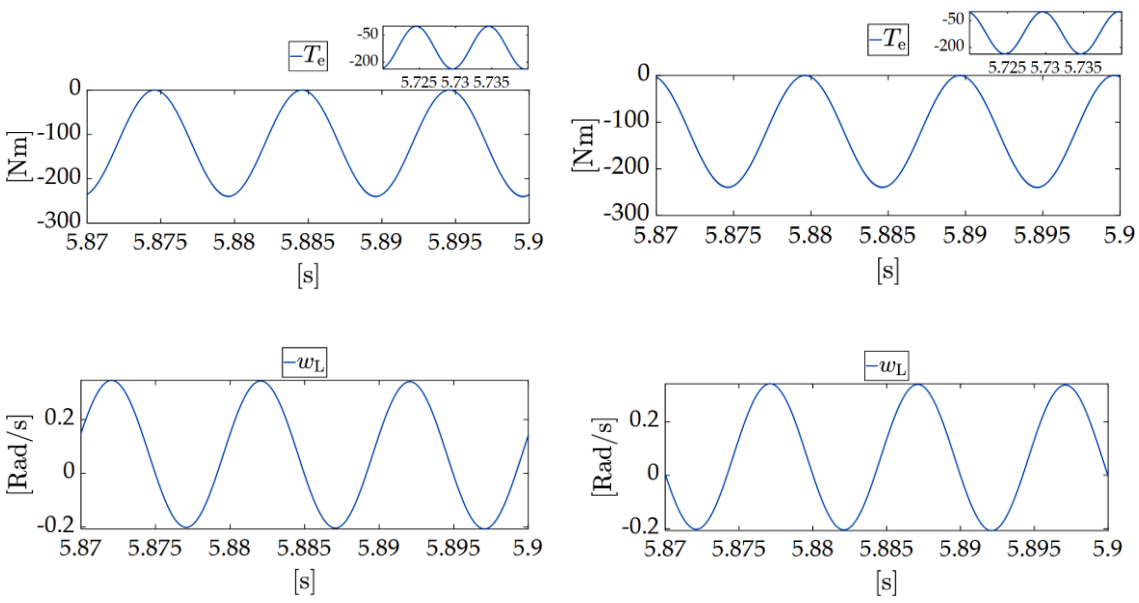


(a) (b)

**Figure 7.** Continued.

**Table 4.** Assumed constants for power loss calculations ([51,52]). This table presents the key electrical, thermal, and magnetic parameters used for estimating power losses and thermal performance in the studied converter topologies. These constants provide a basis for evaluating conduction losses, switching losses, core losses, and copper losses.

| Variable | Description | Values |
|---|---|---|
| $V_{dc}$ | DC-link voltage | 800 (V) |
| $I_{load}$ | Load current | 15 (A) |
| $f_{sw}$ | Switching frequency | 10 (kHz) |
| $R_{on}$ | On-state resistance per switch | 0.08 (Ω) |
| $t_{on}$ | Turn-on time | 80 (ns) |
| $t_{off}$ | Turn-off time | 80 (ns) |
| $R_{winding}$ | Winding resistance per phase | 0.04 (Ω) |
| $k$ | Material constant for core loss estimation | 0.002 |
| $\alpha$ | Frequency exponent (Steinmetz equation) | 1.6 |
| $\beta$ | Flux density exponent (Steinmetz equation) | 2.3 |
| $B_{max}$ | Maximum flux density | 0.35 (T) |
| $V_{core}$ | Core volume | 0.0006 ($m^3$) |
| $R_{th\text{-}jc}$ | Junction-to-case thermal resistance | 0.6 (℃/W) |
| $T_c$ | Case temperature | 50 (℃) |

From the results in Table 5, the thermal analysis of the 2L-1P-NPC, 3L-1P-NPC, and 4L-1P-NPC converters reveals critical trade-offs between conduction losses, switching losses, total power dissipation, and thermal performance. As the number of converter levels increases, conduction losses ($P_{cond}$) scale linearly due to the greater number of power semiconductor devices, reaching 144 W in the 4L-1P-NPC converter. Although multilevel converters reduce per-device switching stress,

the overall switching losses ($P_{sw}$) escalate significantly, with the 4L-1P-NPC converter dissipating nearly twice the energy of the 2L-1P-NPC converter. Core and copper losses remain stable, suggesting that the passive component design is less affected by the converter's topology but still requires optimization for efficiency. The total power loss ($P_{total}$) rises sharply, resulting in higher junction temperatures ($T_j$), which peak at 188 ℃ in the 4L-1P-NPC converter, raising concerns about thermal runaway and long-term reliability. These findings emphasize the necessity of advanced cooling solutions, such as forced-air or liquid cooling, to ensure safe operation in higher-level converters. While multilevel converters improve the harmonic performance and dynamic response, their increased thermal demands necessitate a careful balance between efficiency, power density, and thermal dissipation strategies.

**Table 5.** Comprehensive power loss and thermal analysis. This table presents the calculated power dissipation components—including conduction losses, switching losses, core losses, and copper losses—for each converter topology. Additionally, the total power loss ($P_{total}$) and resulting junction temperature ($T_j$) are provided, highlighting the thermal impact of increasing converter levels and the necessity of effective heat dissipation strategies.

| Topology | $P_{cond}$ (W) | $P_{sw}$ (W) | $P_{core}$ (W) | $P_{copper}$ (W) | $P_{total}$ (W) | $T_j$ (℃) |
|---|---|---|---|---|---|---|
| **2L-1P-NPC** | 72 | 38.4 | 0.27 | 9 | 119.67 | 121.8 |
| **3L-1P-NPC** | 108 | 57.6 | 0.27 | 9 | 174.87 | 154.9 |
| **4L-1P-NPC** | 144 | 76.8 | 0.27 | 9 | 230.07 | 188 |

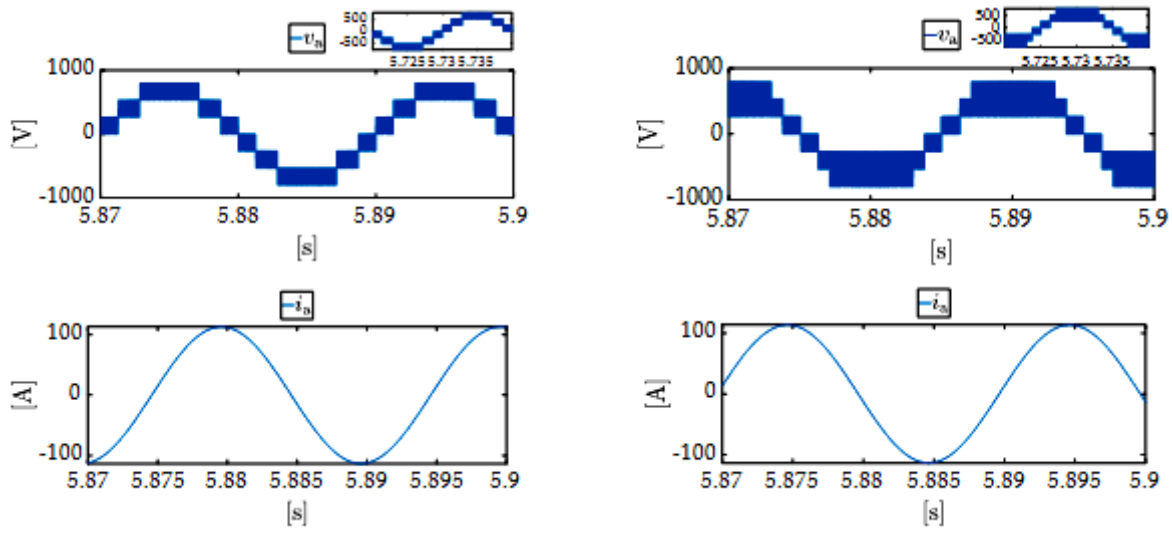


(a) (b)

**Figure 8.** Steady-state simulation results for Topology C (4L-1P-NPC) under different modulation scenarios. The system is initialized with a mechanical load position of $\theta_{L0} = 0°$ and an angular velocity of $\omega_{L0} = 0$ rad/s. The figure illustrates the converter dynamics, including the DC-side current $i_{dc2}(t)$ and duty ratios $d_{11}(t)$ and $d_{12}(t)$ for Leg 1, along with the SPRM's electrical variables $v_a(t)$, $i_a(t)$, and electromagnetic torque $T_e(t)$. The mechanical response $\omega_L(t)$ is also depicted. (a) Scenario 3. (b) Scenario 4.

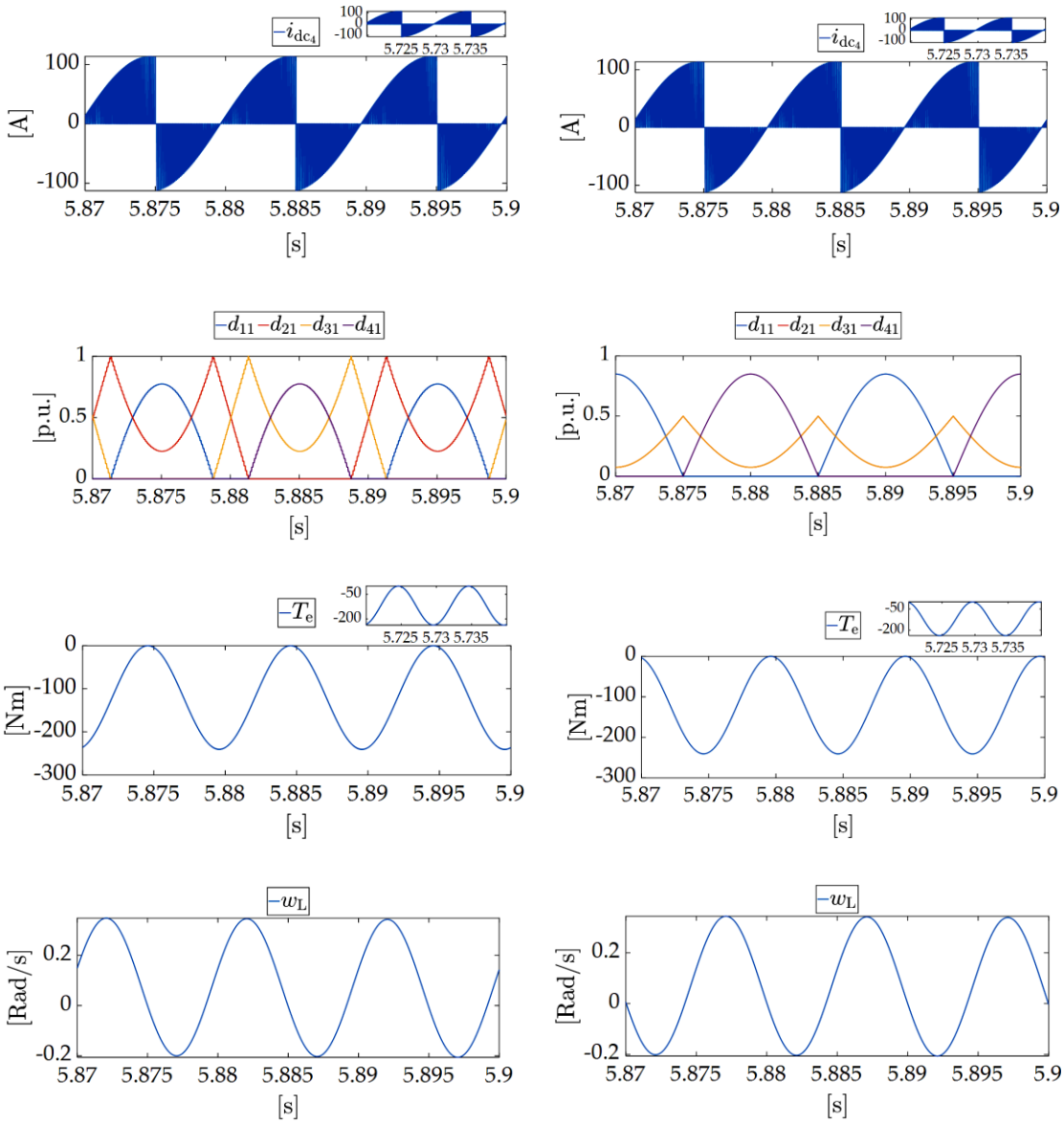


**Figure 8.** Continued.

This enhanced simulation framework offers critical insights into the interdependence among modulation schemes, converter topologies, harmonic content, thermal characteristics, and transient control behavior. These results validate the comprehensive effectiveness of multilevel converters in advanced motor drive systems, establishing a strong foundation for subsequent experimental implementation.

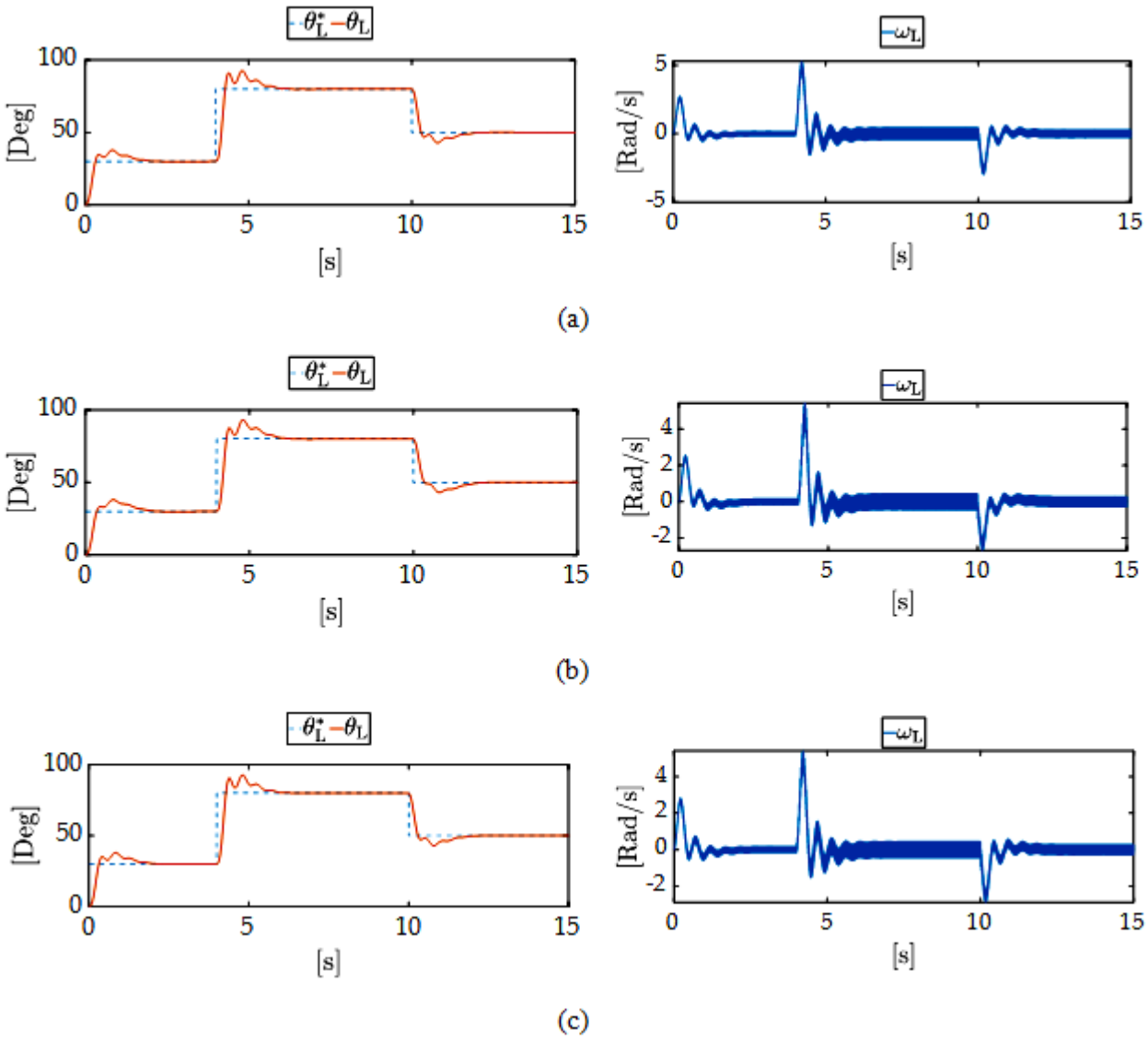


**Figure 9.** Transient response of the mechanical load position control and angular velocity under different converter topologies. The system is initialized with a mechanical load position of $\theta_{L0}$ = 0° and an angular velocity of $\omega_{L0}$ = 0 rad/s. A step change in the reference position $\theta_L^*$(t) is applied at $t$ = 4 s and $t$ = 10 s, evaluating the system's dynamic performance. The figure presents the transient response for (a) Topology A (2L-1P-NPC) under Scenario 2, (b) Topology B (3L-1P-NPC) under Scenario 4, and (c) Topology C (4L-1P-NPC) under Scenario 4.

## 8. Conclusions

This study presented a rigorous simulation-based evaluation of the harmonic, dynamic, and thermal performance of SPRM drives using multilevel NPC DC–AC converters. Three converter topologies—2L-1P-NPC, 3L-1P-NPC, and 4L-1P-NPC—were systematically analyzed under various modulation schemes to assess their impact on THD, electromagnetic torque ripple, transient response, and power loss distribution. High-fidelity simulations incorporating realistic motor and mechanical load parameters demonstrated that increasing the converter level significantly enhances

harmonic quality. Notably, the 4L-1P-NPC topology with LSPWM achieved the lowest output voltage THD (23.66%) and electromagnetic torque THD (0.17%), effectively minimizing torque ripple and mitigating deleterious effects such as acoustic noise and mechanical vibrations.

In addition to harmonic improvements, the study reveals that multilevel topologies yield superior dynamic performance. The transient response metrics—rise time, settling time, overshoot, and steady-state error—clearly improve with the converter level, with the 4L-1P-NPC converter exhibiting a 0.24 s rise time and only 0.1 ° of steady-state error. These enhancements are critical for high-precision motion applications where dynamic response and control stability are essential. Furthermore, a quantitative thermal analysis indicates that higher-level topologies, while beneficial in the harmonic and control domains, impose increased thermal stress due to cumulative conduction and switching losses. For instance, junction temperature rises from 121.8 ℃ in the 2L topology to 188 ℃ in the 4L configuration, underscoring the importance of implementing advanced thermal management strategies to ensure long-term reliability.

Overall, this research contributes a comprehensive design and analysis framework that integrates harmonic distortion mitigation, dynamic control validation, and thermal feasibility for SPRM-based drive systems. These findings offer valuable guidance for the development of high-performance, thermally robust, and harmonically optimized converter-driven motor applications. Future work will focus on experimental validation and the development of real-time control platforms to translate these theoretical insights into practical implementations.

## Author contributions

José M. Campos-Salazar: Conceptualization, methodology, validation, formal analysis, investigation, writing—original draft, supervision; Roya Rafiezadeh: Methodology, validation, formal analysis, investigation, writing—review and editing; Juan L. Aguayo-Lazcano: Methodology, validation, formal analysis, investigation, writing—review and editing; Constanza Márquez: validation, formal analysis, investigation, writing—review and editing.

## Use of Generative AI tools declaration

The authors declare they have not used artificial intelligence (AI) tools in the creation of this article.

## Conflict of interest

All authors declare no conflicts of interest in this paper.

## References

1. Singh GK (2005) A Research Survey of Induction Motor Operation with Non-Sinusoidal Supply Wave Forms. *Electr Pow Syst Res* 75: 200–213. https://doi.org/10.1016/j.epsr.2005.04.001
2. Timár-P L (1989) *Noise and Vibration of Electrical Machines*; Elsevier.
3. Wallace AK, Spee R, Martin LG (1990) Current Harmonics and Acoustic Noise in AC Adjustable-Speed Drives. *IEEE T Ind Appl* 26: 267–273. https://doi.org/10.1109/28.54252

4. Belmans RJM, D'Hondt L, Vandenput AJ, Geysen W (1987) Analysis of the Audible Noise of Three-Phase Squirrel-Cage Induction Motors Supplied by Inverters. *IEEE T Ind Appl* IA-23: 842–847. https://doi.org/10.1109/TIA.1987.4504993
5. Iida S, Okuma Y, Masukawa S, Miyairi S, Bose BK (1991) Study on Magnetic Noise Caused by Harmonics in Output Voltages of PWM Inverter. *IEEE T Ind Electronic* 38: 180–186. https://doi.org/10.1109/41.87585
6. Habetler TG, Divan DM (1991) Acoustic Noise Reduction in Sinusoidal PWM Drives Using a Randomly Modulated Carrier. *IEEE T Power Electr* 6: 356–363. https://doi.org/10.1109/63.85902
7. Blaabjerg F, Pedersen JK, Ritchie E, Nielsen P (1995) Determination of Mechanical Resonances in Induction Motors by Random Modulation and Acoustic Measurement. *IEEE T Ind Appl* 31: 823–829. https://doi.org/10.1109/28.395292
8. Grant D, Houldsworth J (1984) PWM AC Motor Drive Employing Ultrasonic Carrier. *Power Electronics and Variable Speed Drives Conference, London*, 237–240.
9. Ueda S, Honda K, Ikimi T, Hombu M, Ueda A (1991) Magnetic Noise Reduction Technique for an AC Motor Driven by a PWM Inverter. *IEEE T Power Electr* 6: 470–475. https://doi.org/10.1109/63.85897
10. Hombu M, Ueda S, Ueda A, Matsuda Y (1985) A New Current Source GTO Inverter with Sinusoidal Output Voltage and Current. *IEEE T Ind Appl* IA-21: 1192–1198. https://doi.org/10.1109/TIA.1985.349523
11. Wang C, Lai JCS, Pulle DWJ (2002) Prediction of Acoustic Noise from Variable-Speed Induction Motors: Deterministic versus Statistical Approaches. *IEEE T Ind Appl* 38: 1037–1044. https://doi.org/10.1109/TIA.2002.800567
12. Yang SJ (1981) *Low-Noise Electrical Motors*, Clarendon Press.
13. Timar PL, Lai JCS (1994) Acoustic Noise of Electromagnetic Origin in an Ideal Frequency-Converter-Driven Induction Motor. *IEE Proceedings - Electric Power Applications* 141: 341–346. https://doi.org/10.1049/ip-epa:19941342
14. Na SH, Jung YG, Lim YC, Yang SH (2002) Reduction of Audible Switching Noise in Induction Motor Drives Using Random Position Space Vector PWM. *IEE Proceedings - Electric Power Applications* 149: 195–200. https://doi.org/10.1049/ip-epa:20020244
15. Xu L, Zhu ZQ, Howe D (2000) Acoustic Noise Radiated from Direct Torque Controlled Induction Motor Drives. *Electric Power Applications, IEE Proceedings* 147: 491–496. https://doi.org/10.1049/ip-epa:20000582
16. Ishibashi F, Kamimoto K, Noda S, Itomi K (2003) Small Induction Motor Noise Calculation. *IEEE T Energy Conver* 18: 357–361. https://doi.org/10.1109/TEC.2002.808415
17. Fitzgerald AE, Kingsley C, Umans SD (2003) *Electric Machinery*, McGraw-Hill.
18. Murphy JMD, Turnbull FG (1988) *Power Electronic Control of AC Motors*, Franklin Book Company, Incorporated.
19. McLean GW, Nix GF, Alwash SR (1969) Performance and Design of Induction Motors with Square-Wave Excitation. *Proceedings of the Institution of Electrical Engineers* 116: 1405–1411. https://doi.org/10.1049/piee.1969.0254
20. Ding K, Cheng KWE, Wang SX, Wang DH, Shi Z (2008) Five-Level Cascaded Multilevel Motor Driver for Electrical Vehicle with Battery Charge Management. In *Proceedings of the 2008 Australasian Universities Power Engineering Conference*, 1–6.

21. Pant GKS (2000) Vinay Analysis of a Multiphase Induction Machine Under Fault Condition in a Phase-Redundant A.C. Drive System. *Electric Machines & Power Systems* 28: 577–590. https://doi.org/10.1080/073135600268199
22. Busquets-Monge S (2018) Neutral-Point-Clamped DC–AC Power Converters. In *Wiley Encyclopedia of Electrical and Electronics Engineering*, 1–20. https://doi.org/10.1002/047134608X.W8365
23. Rasilo P, Salem A, Abdallh A, De Belie F, Dupré L, Melkebeek JA (2015) Effect of Multilevel Inverter Supply on Core Losses in Magnetic Materials and Electrical Machines. *IEEE T Energy Conver* 30: 736–744. https://doi.org/10.1109/TEC.2014.2372095
24. Mahmoud H, Bacco G, Degano M, Bianchi N, Gerada C (2018) Synchronous Reluctance Motor Iron Losses: Considering Machine Nonlinearity at MTPA, FW, and MTPV Operating Conditions. *IEEE T Energy Conver* 33: 1402–1410. https://doi.org/10.1109/TEC.2018.2811543
25. Liu CT, Lai YS, Yen SC, Lin HN, Hsu YW, Luo TY, et al. (2022) Design of High-Efficiency Single-Phase Direct-on-Line Synchronous Reluctance Motors for Pump Applications. *IEEE T Ind Appl* 58: 5480–5487. https://doi.org/10.1109/TIA.2022.3164020
26. Nasar SA (1990) *Schaum's Outline of Electrical Power Systems*, McGraw Hill Professional.
27. Houpis CH, Sheldon SN, D'Azzo JJ (2003) *Linear Control System Analysis and Design: Fifth Edition, Revised and Expanded*, CRC Press.
28. Park RH (1929) Two-Reaction Theory of Synchronous Machines Generalized Method of Analysis-Part I. *Transactions of the American Institute of Electrical Engineers* 48: 716–727. https://doi.org/10.1109/T-AIEE.1929.5055275
29. Mohan N (1995) *Power Electronics: Converters, Applications, and Design*, Wiley.
30. Bordonau J, Cosan M, Borojevic D, Mao H, Lee FC (1997) A State-Space Model for the Comprehensive Dynamic Analysis of Three-Level Voltage-Source Inverters. In *Proceedings of the PESC97. Record 28th Annual IEEE Power Electronics Specialists Conference. Formerly Power Conditioning Specialists Conference 1970-71. Power Processing and Electronic Specialists Conference 1972,* 2: 942–948. https://doi.org/10.1109/PESC.1997.616837
31. Menéndez SSA (2004) *Aportación al control del convertidor CC/CA de tres niveles*.
32. Guerrero JM, Garcia de Vicuna L, Miret J, Matas J, Castilla M (2002) A Nonlinear Feed-Forward Control Technique for Single-Phase UPS Inverters. In *Proceedings of the IEEE 2002 28th Annual Conference of the Industrial Electronics Society. IECON 02,* 1: 257–261. https://doi.org/10.1109/IECON.2002.1187517
33. Holtz J (1992) Pulsewidth Modulation-a Survey. *IEEE T Ind Electron* 39: 410–420. https://doi.org/10.1109/41.161472
34. Vedith S, Bhanu Tej JN, Sampath S, Usha Sree M, Nithin Rao P, Neelima K (2022) Review on Pulse Width Modulation and Optimization Techniques for Multilevel Inverters. In *Proceedings of the International Conference on Artificial Intelligence and Sustainable Engineering; Sanyal, G., Travieso-González, C.M., Awasthi, S., Pinto, C.M.A., Purushothama, B.R., Eds.; Springer Nature: Singapore,* 235–249. https://doi.org/10.1007/978-981-16-8542-2_19
35. Busquets-Monge S, Bordonau J, Boroyevich D, Somavilla S (2004) The Nearest Three Virtual Space Vector PWM - a Modulation for the Comprehensive Neutral-Point Balancing in the Three-Level NPC Inverter. *IEEE Power Electronics Letters* 2: 11–15. https://doi.org/10.1109/LPEL.2004.828445
36. Busquets-Monge S (2022) A Simple Virtual-Vector-Based PWM Formulation for Multilevel

Three-Phase Neutral-Point-Clamped DC–AC Converters Including the Overmodulation Region. *Electronics* 11: 641. https://doi.org/10.3390/electronics11040641
37. Busquets-Monge S, Alepuz S, Rocabert J, Bordonau J (2009) Pulsewidth Modulations for the Comprehensive Capacitor Voltage Balance of $n$-Level Three-Leg Diode-Clamped Converters. *IEEE T Power Electr* 24: 1364–1375. https://doi.org/10.1109/TPEL.2009.2016661
38. Busquets-Monge S, Maheshwari R, Nicolas-Apruzzese J, Lupon E, Munk-Nielsen S, Bordonau J (2015) Enhanced DC-Link Capacitor Voltage Balancing Control of DC–AC Multilevel Multileg Converters. *IEEE T Ind Electron* 62: 2663–2672. https://doi.org/10.1109/TIE.2014.2363820
39. Busquets-Monge S, Ruderman A (2010) Carrier-Based PWM Strategies for the Comprehensive Capacitor Voltage Balance of Multilevel Multileg Diode-Clamped Converters. In *Proceedings of the 2010 IEEE International Symposium on Industrial Electronics*, 688–693. https://doi.org/10.1109/ISIE.2010.5637187
40. Ramu V, Satish Kumar P, Srinivas GN (2022) LSPWM, PSPWM and NLCPWM on Multilevel Inverters with Reduced Number of Switches. *Materials Today: Proceedings* 54: 710–727. https://doi.org/10.1016/j.matpr.2021.10.410
41. Hammami M, Vujacic M, Grandi G (2018) Dc-Link Current and Voltage Ripple Harmonics in Three-Phase Three-Level Flying Capacitor Inverters with Sinusoidal Carrier-Based PWM. *2018 IEEE International Conference on Industrial Technology (ICIT)*, 664–669. IEEE. https://doi.org/10.1109/ICIT.2018.8352257
42. Angulo M, Lezana P, Kouro S, Rodriguez J, Wu B (2007) Level-Shifted PWM for Cascaded Multilevel Inverters with Even Power Distribution. In *Proceedings of the 2007 IEEE Power Electronics Specialists Conference*, 2373–2378. https://doi.org/10.1109/PESC.2007.4342382
43. Garcia-Reyes LA, Beltrán-Telles A, Bañuelos-Ruedas F, Reta-Hernández M, Ramírez-Arredondo JM, Silva-Casarín R (2022) Level-Shift PWM Control of a Single-Phase Full H-Bridge Inverter for Grid Interconnection, Applied to Ocean Current Power Generation. *Energies* 15: 1644. https://doi.org/10.3390/en15051644
44. Kishor Y, Patel RN (2022) Thermal Modelling and Reliability Analysis of Recently Introduced High Gain Converters for PV Application. *Cleaner Energy Systems* 3: 100016. https://doi.org/10.1016/j.cles.2022.100016
45. Plesca A (2011) Thermal Analysis of Power Semiconductor Converters. In *Power Quality Harmonics Analysis and Real Measurements Data*. IntechOpen. https://doi.org/10.5772/16407
46. Erickson RW (2013) *Fundamentals of Power Electronics*, Springer Science & Business Media.
47. Vasin A, Kocherov A, Okunev A (2021) Thermal Analysis of Power MOSFETS in Boost DC/DC Converter. In *Proceedings of the 2021 International Russian Automation Conference (RusAutoCon)*, 474–479. https://doi.org/10.1109/RusAutoCon52004.2021.9537406
48. Ogata K (2009) *Modern Control Engineering*, 5th edition, Pearson: Boston.
49. Andrade DA, de Freitas MA, Neto LM, Paula HD, Domingos JL (2004) Effects of Magnetic Saturation on Induction Machines Driven by Static Converters. *Sba Controle & Automação* 15: 181–189. https://doi.org/10.1590/S0103-17592004000200007
50. Kuo BC (1991) *Automatic Control Systems*, 6th edition, Prentice Hall: Englewood Cliffs, N.J.
51. Hahn F, Andresen M, Buticchi G, Liserre M (2018) Thermal Analysis and Balancing for Modular Multilevel Converters in HVDC Applications. *IEEE T Power Electron* 33: 1985–1996. https://doi.org/10.1109/TPEL.2017.2691012

52. Liu Y, Sheng J, Dong Y, Zheng R, Li W, He X, et al. (2018) Thermal Analysis of Modular Multilevel Converters Under Subsynchronous Oscillation. In *Proceedings of the 2018 IEEE Energy Conversion Congress and Exposition (ECCE)*, 5190–5195. https://doi.org/10.1109/ECCE.2018.8558414


AIMS Press